

Supporting Information

Phosphorus-Mediated MoS₂ Nanowires as a High-Performance Electrode Material for Quasi-Solid-State Sodium-Ion Intercalation Supercapacitors

Shude Liu,¹ Ying Yin,^{1, 2} Musheng Wu,³ Kwan San Hui,⁴ Kwun Nam Hui,^{*,5} Chu-Ying Ouyang,^{*,3} and Seong Chan Jun^{*,1}

¹School of Mechanical Engineering, Yonsei University, Seoul 120-749, South Korea.

²Guangxi Key Laboratory of Information Materials, Guilin University of Electronic Technology, Guilin 541004, PR China.

³Department of Physics, Jiangxi Normal University, Nanchang, 330022, China.

⁴School of Mathematics, University of East Anglia, Norwich, NR4 7TJ, United Kingdom.

⁵Institute of Applied Physics and Materials Engineering, University of Macau, Avenida da Universidade, Taipa, Macau, China.

*Corresponding author's E-mail: bizhui@umac.mo; cyouyang@jxnu.edu.cn; scj@yonsei.ac.kr

Experimental section

Materials synthesis

Synthesis of ethylenediamine trimolybdate ($\text{MoO}_3\text{-EDA}$) inorganic-organic hybrid nanostructure

The $\text{MoO}_3\text{-EDA}$ was synthesized following a previous report with minor modification.^[1] Briefly, we dissolved $(\text{NH}_4)_6\text{Mo}_7\text{O}_2\cdot 4\text{H}_2\text{O}$ (2.48 g) and aniline (3.34 g) in distilled water (50 mL) to form a homogenous solution. Then, 1 M HCl solution was added dropwise with constant stirring until white precipitation formed (pH=4–5). The stirring was continued at 50 °C for 2 h. The precipitate was collected and rinsed with deionized water and ethanol several times, and then dried in an oven at 70 °C for 24 h.

Synthesis of MoS_2 nanowires

The obtained $\text{MoO}_3\text{-EDA}$ (0.25 g) was dispersed in a homogenous solution containing ethanol (50 mL) and thioacetamide (0.4 g). The dispersion solution was subsequently transferred to 100 mL Teflon-lined stainless-steel autoclaves and maintained at 160 °C, 180 °C, and 200 °C for 12 h. The obtained samples were rinsed with ethanol and water and oven-dried at 70 °C for 12 h. The resultant MoS_2 composites with different temperatures (160 °C, 180 °C, and 200 °C) were denoted as $\text{MoS}_2\text{-}160\text{ }^\circ\text{C}$, $\text{MoS}_2\text{-}180\text{ }^\circ\text{C}$, and $\text{MoS}_2\text{-}200\text{ }^\circ\text{C}$, respectively. We performed an annealing process at 200 °C for 2 h under Ar to increase the crystallinity.

Synthesis of P-doped MoS_2 nanowires

To prepare P-doped MoS₂ further, the quartz boat with MoS₂-180 °C (0.15 g) and NaH₂PO₂·H₂O (0.15 g) were loaded into a two-zone tube furnace under an Ar flow of 50 cm³ min⁻¹, in which NaH₂PO₂·H₂O was placed in the front zone heated from 20 to 350 °C at a heating rate of 5 °C/min and kept at this temperature for 2 h. MoS₂ was placed in the back zone heated from 20 to 700 °C at a heating rate of 10 °C/min and kept at this temperature for 2 h.

Synthesis of MnO₂ nanorods

The MnO₂ nanorods were prepared via a redox reaction under the hydrothermal process. Typically, 0.394 g KMnO₄ and 0.777 g MnSO₄·6 H₂O were dissolved in 40 mL of distilled water with vigorous stirring to form a homogeneous solution. The resultant solution was transferred into a Teflon-lined stainless steel autoclave and maintained at 150 °C for 2 h. After naturally cooling to room temperature, the product precipitate was washed with ethanol several times and dried in an oven at 70 °C for 12 h.

Materials characterization

XRD patterns were recorded on a Rigaku Ultima X-ray diffractometer equipped with Cu K α radiation (XRD; SmartLab; $\lambda = 1.5418\text{\AA}$). The morphologies and structures were characterized by field-emission scanning electron microscopy (FESEM; JEOL-7800F; JEOL) and transmission electron microscopy (TEM; JEM-2010; JEOL) equipped with an energy-dispersive X-ray spectrometer that operated at 200 kV. Raman spectroscopy was collected with a micro-Raman spectrometer LabRAM HR

equipped with a laser excitation wavelength of 514.5 nm. X-ray photoelectron spectrometer (XPS; Thermo Scientific ESCALAB 250; Thermo UK) measurements were performed with monochromatic Al K α radiation as a radiation source to invest the surface states. The electrical conductivity of the sample pellets pressed from powder was performed on a Keithley-2450 source meter using the four-point probe method. The Brunauer–Emmett–Teller (BET) surface area was performed using a nitrogen adsorption analyzer (Autosorb-iQ 2ST/MP, Quantachrome) and the pore-size distribution was determined by the Barrett-Joyner-Halenda method.

Electrochemical measurements

Electrochemical measurements were conducted on an Ivium-n-Stat electrochemical workstation (Ivium, Netherlands) with a three-electrode mode in a 1 M Na₂SO₄ electrolyte. The working electrodes were made through a slurry-coated on nickel foam (NF) procedure. The slurry was composed of an active material, acetylene black, and polyvinylidene fluoride (PVDF) with a mass ratio of 85:10:5 dissolved in ethanol. The loading mass of materials coated on nickel foam (area = 1×1 cm²) was approximately 2.1 mg cm⁻². The electrodes were dried in a vacuum oven at 60 °C for 12 h. The platinum wire and saturated calomel electrode (SCE) were used as counter and reference electrodes, respectively. Electrochemical impedance spectroscopy (EIS) curves were recorded in the frequency range of 0.01 Hz to 100 kHz with an alternating current amplitude of 5 mV. Specific capacitance (C, F g⁻¹) was calculated from the charging/discharging profiles by the following equation:^[2]

$$C = \frac{2I}{m \Delta V^2} \int_{t_1}^{t_2} V dt, \quad (1)$$

where I (A) is the discharging current, m (g) is the mass of the active materials, ΔV (V) is the potential window, t_1 and t_2 are the initial and terminal times of the discharge curve, respectively, and V (V) is the operating potential.

Prior to the assembly of the asymmetric supercapacitor (ASC) device, the mass of the positive electrode material (m_+) and negative electrode material (m_-) was balanced following charge balance theory.^[3]

$$\frac{m_+}{m_-} = \frac{C_- \times V_-}{C_+ \times V_+} . \quad (2)$$

The ASC device was assembled by using P-doped MoS₂ as the positive electrode and MnO₂ as the negative electrode with polyvinyl alcohol (PVA)/Na₂SO₄ gel electrolyte. The energy density (E, W h kg⁻¹) and power density (P, W kg⁻¹) were calculated from current charging/discharging curves using the following equations.^[4]

$$E = \frac{I \int_0^{t_s} V_s dt}{3.6 \cdot M} , \quad (3)$$

$$P = \frac{3600 \times E}{t} , \quad (4)$$

where I , C_s , t_s and V_s are the discharge current (A), specific capacitance (F g⁻¹) based on the total mass (M, g) of negative and positive electrode materials, the discharge time (s), and the operating voltage of discharge process for ASC device.

Density functional theory (DFT) calculations

Computational details

All theoretical calculations were conducted with DFT with Projector Augmented Wave (PAW) pseudopotentials,^[5] as implemented in the Vienna *ab initio* simulation package (VASP) code.^[6] The electron exchange-correlation energy was described in the generalized gradient approximation (GGA) using the Perdew–Burke–Ernzerhof (PBE) prescription.^[7] The cutoff energy of 550 eV was used for the plane waves. The lattice parameters and the ionic positions are fully relaxed, and the final forces on each atom were 0.01 eV/Å. The calculation of density of states (DOS) was smeared by the Gaussian smearing method with a smearing width of 0.05 eV. The Monkhorst–Pack type of k -point sampling was used.^[8] The density of the k -mesh is thicker than 0.03 Å⁻¹, and the vacuum space along the z direction was higher than 15 Å. The DFT-D3 correction of Grimme was used for the dispersion interactions.^[9] The Na⁺ ion diffusion path and the minimum energy barriers were determined through the climbing image nudged elastic band (CINEB) method.^[10]

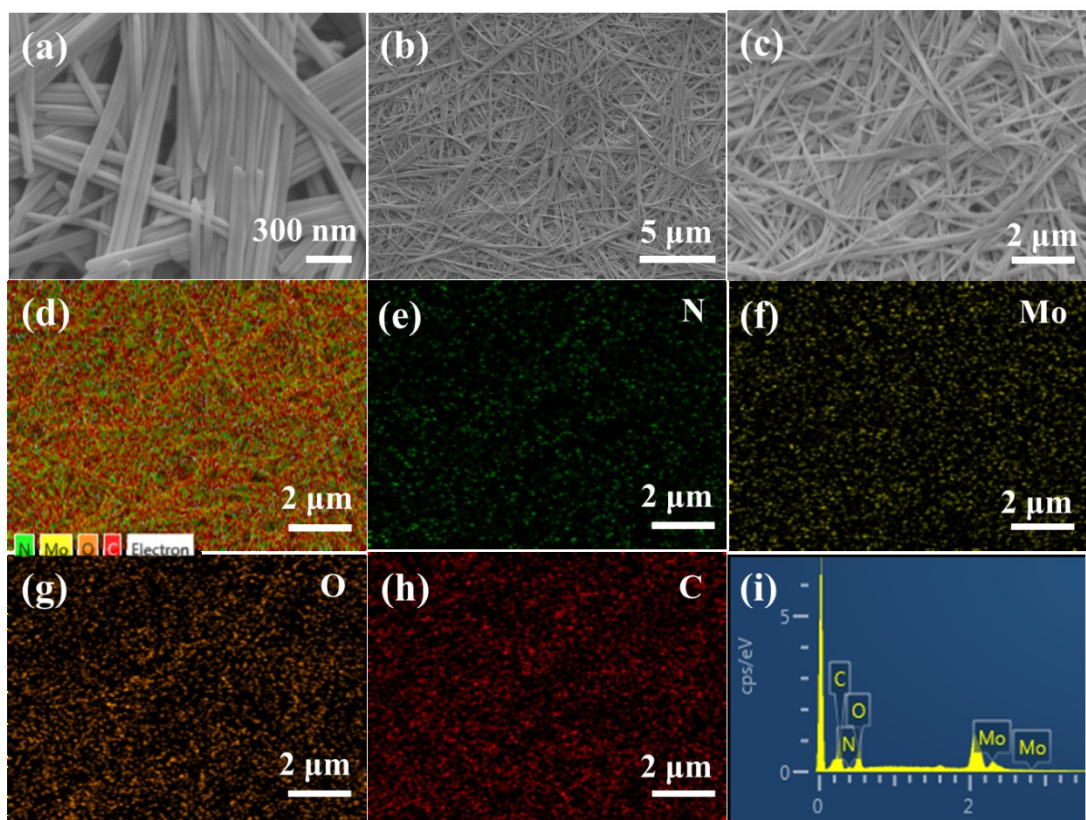


Figure S1. (a–c) SEM images of MoO₃-EDA nanowires at different magnifications. (d–g) EDS elemental mappings of N, Mo, O, and C elements recorded from image (c), and (i) the corresponding EDS spectrum.

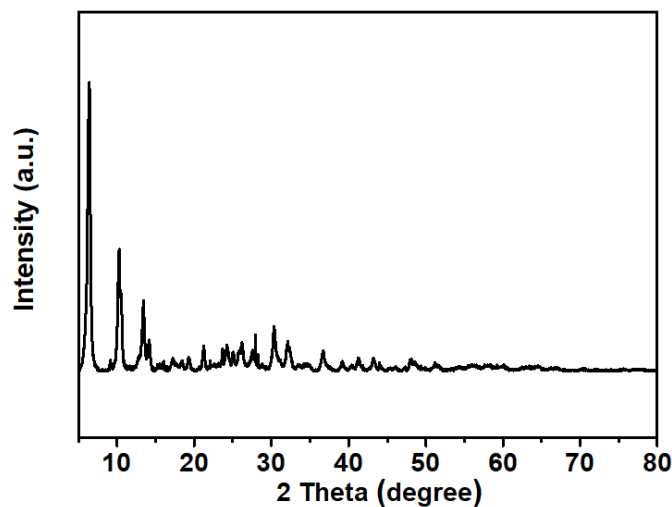


Figure S2. XRD pattern of MoO₃-EDA nanowires.

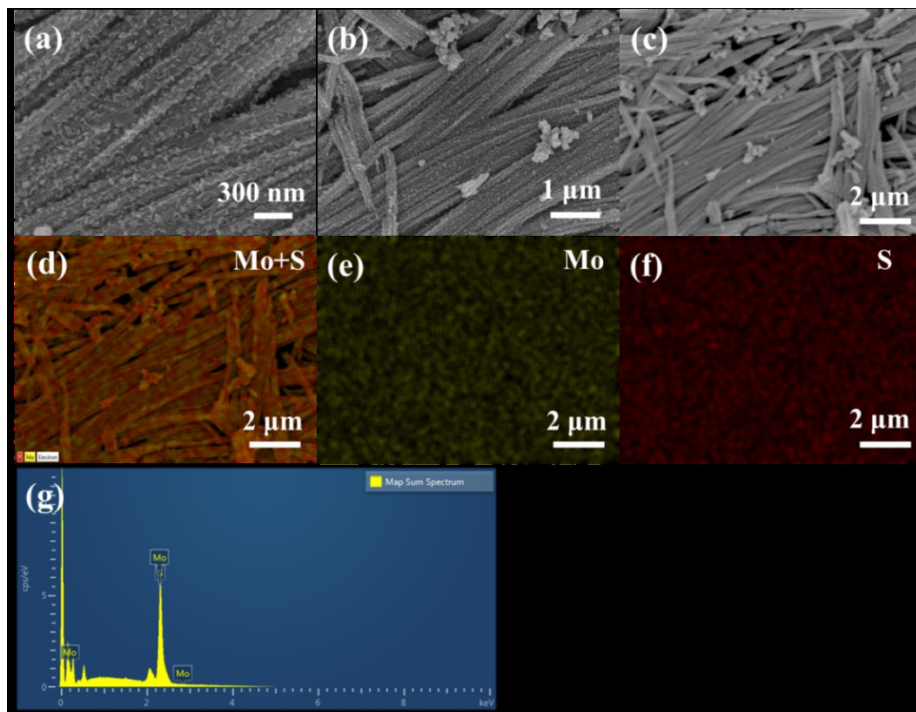


Figure S3. (a–c) SEM images of MoS₂-180 °C nanostructures at different magnifications. (d–g) EDS elemental mappings of Mo and S elements recorded from image (c), and (h) the corresponding SEM-EDS spectrum and atomic percentages.

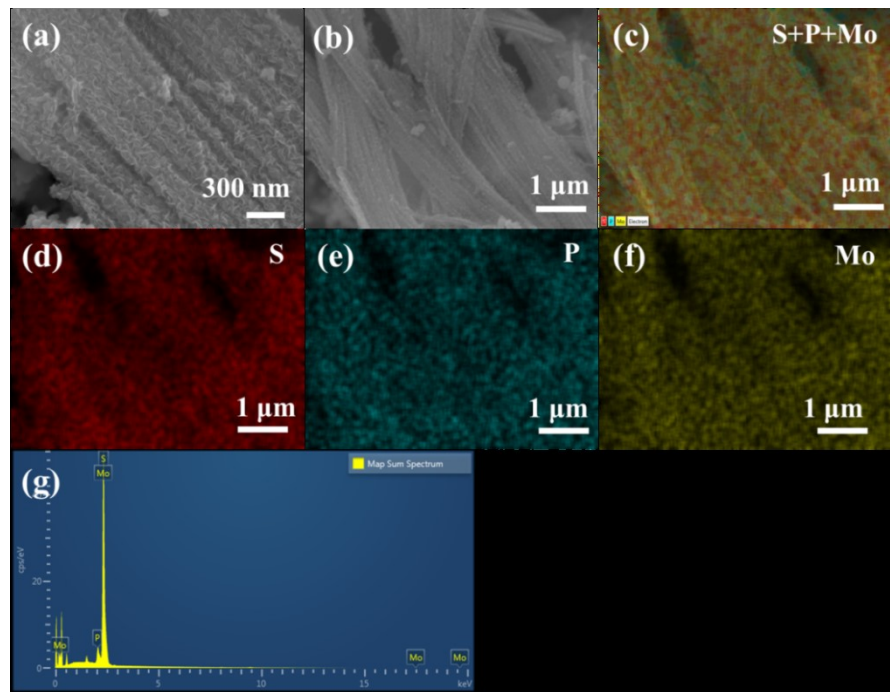


Figure S4. (a) SEM image of P-doped MoS₂ nanostructure, (b–f) the EDS elemental mappings of P, Mo, and S elements recorded from image (b), and (g) the corresponding SEM-EDS spectrum and elemental percentages.

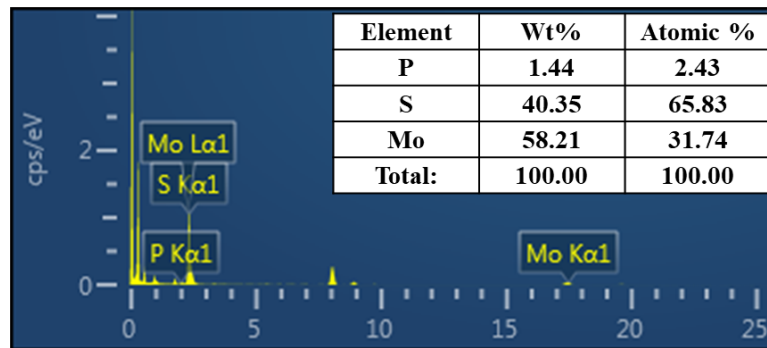


Figure S5. EDS spectrum from TEM-EDS analysis, and corresponding mass and atomic percentage of P-doped MoS₂ nanostructure.

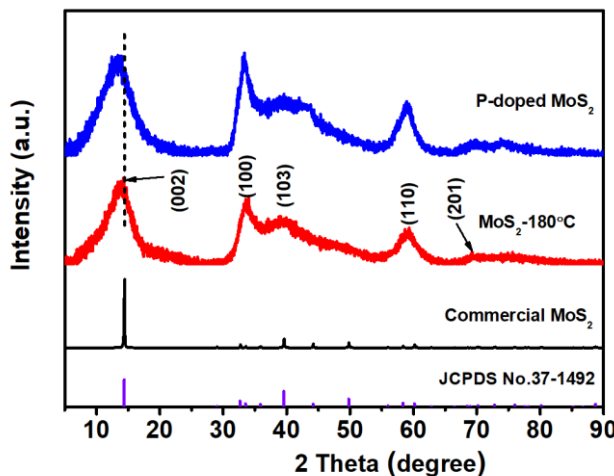


Figure S6. (a) XRD patterns of commercial bulk MoS₂, MoS₂-180 °C and P-doped MoS₂.

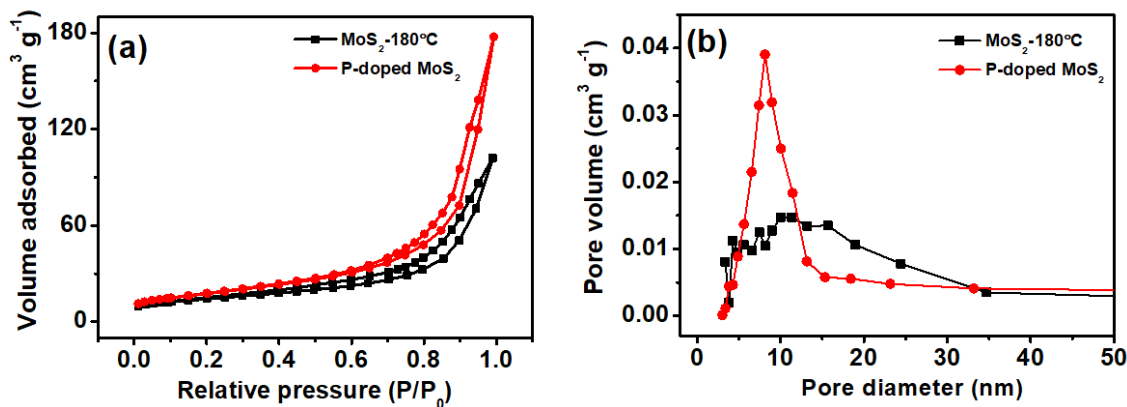


Figure S7. (a) N₂ adsorption–desorption isotherms, and (b) the pore size distribution MoS₂-180 °C and P-doped MoS₂.

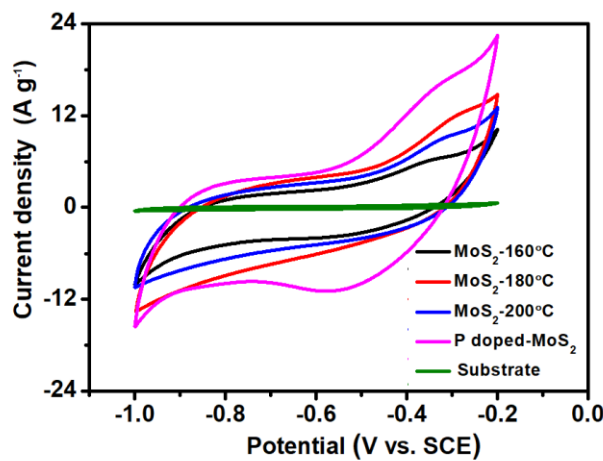


Figure S8. Comparative CV curves of MoS_2 (160 °C, 180 °C, and 200 °C), P-doped MoS_2 , and Ni substrate at a scan rate of 20 mV s^{-1} .

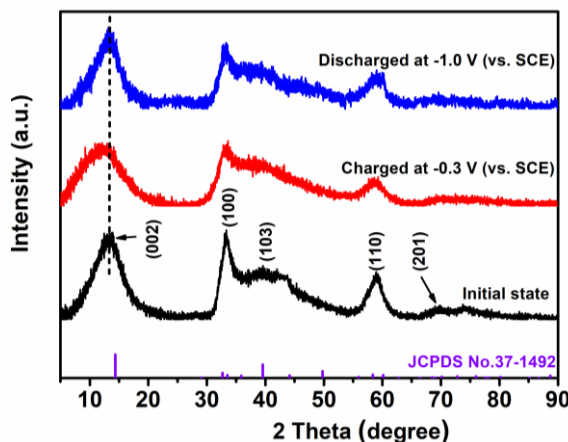


Figure S9. Ex-situ XRD patterns of P-doped MoS_2 at different cut off potentials.

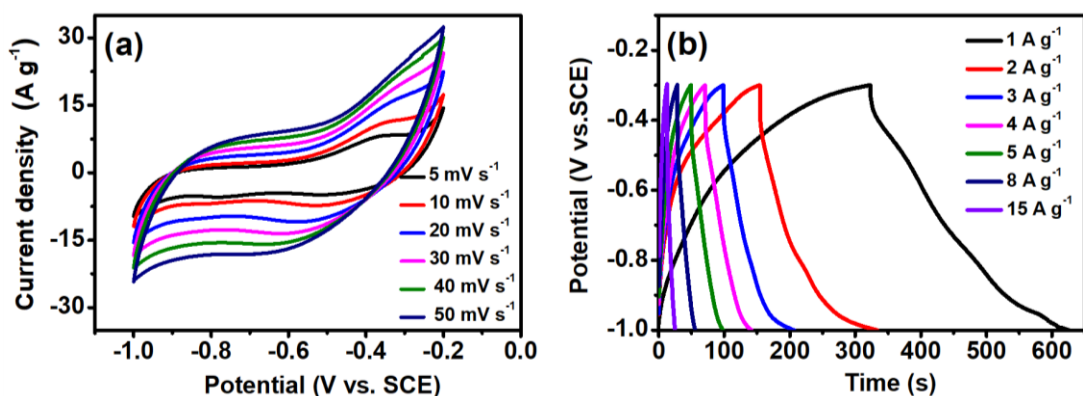


Figure S10. (a) CV curves at different scan rates, and (b) GCD curves at different current densities for P-doped MoS_2 .

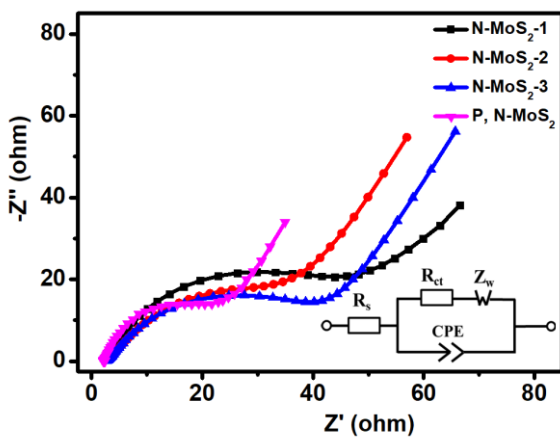


Figure S11. Nyquist plot of electrochemical impedance spectra for MoS₂ (160 °C, 180 °C, and 200 °C) and P-doped MoS₂.

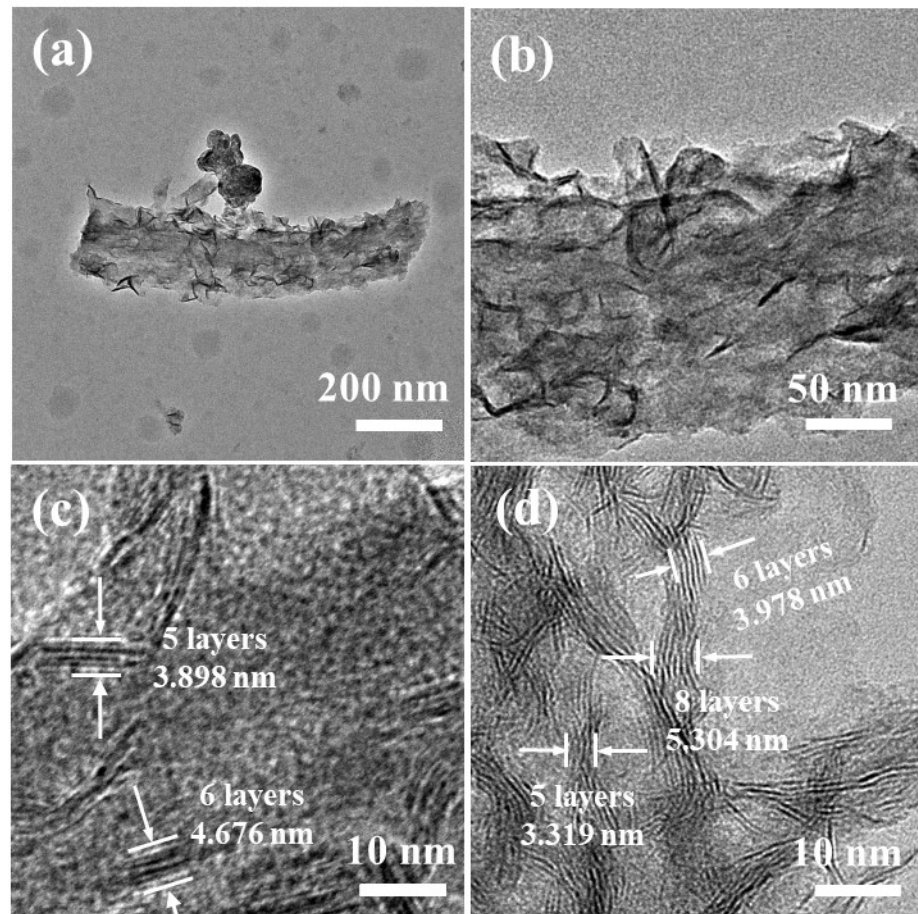


Figure S12. (a–c) TEM images after cycling, and (d) TEM image before cycling for homogenous P-doped MoS₂ nanowires.

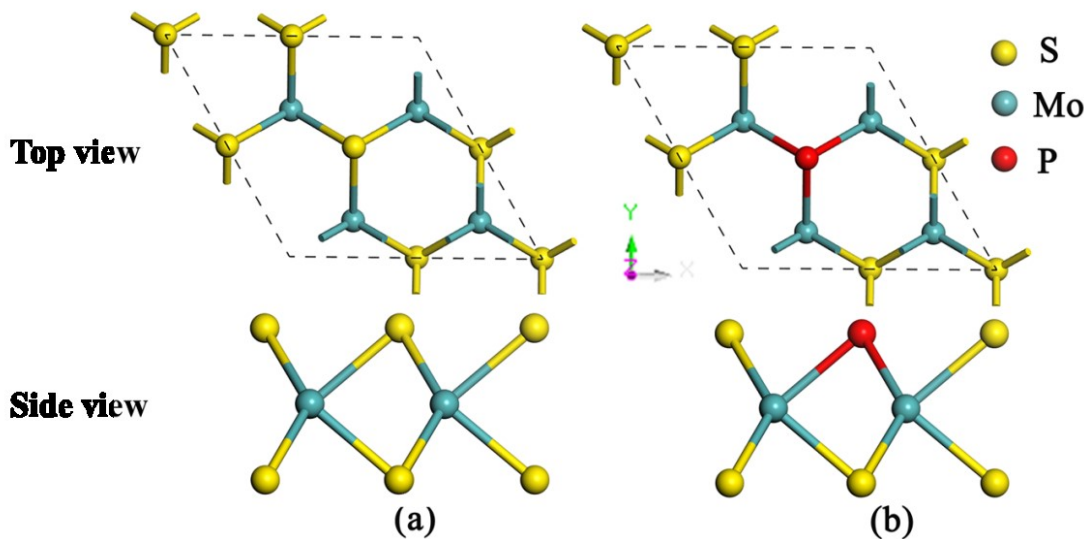


Figure S13. Top and side views of (a) 2H-MoS₂ and (b) P-doped MoS₂.

Structural models

The 2H phase is the ground state for monolayer MoS₂ and more stable than the 1T phase.^[11] We developed the model of P-doped MoS₂ on the basis of the 2H-MoS₂ structure. First, the primitive unit cell of 2H-MoS₂ was fully optimized. The corresponding lattice constants are $a=b=3.166$ Å, in agreement with previous results.^[12] Then, a $2\times 2\times 1$ supercell of 2H-MoS₂ is constructed. Finally, one S atom is replaced with one P atom, thereby generating the P-doping concentration of 12.5%. The geometry structures of pure 2H-MoS₂ and P-doped MoS₂ are shown in Figure S12.

Na⁺ ion intercalation on MoS₂ and P-doping MoS₂

To investigate the specific capacitance of Na⁺ ion intercalation on monolayer MoS₂, we must determine the most stable Na-adsorption configuration of one Na⁺ ion on the host structures, whether pure or P-doped. Thus, we modeled larger supercells for pure

MoS_2 (including 32 S and 16 Mo atoms) and P-doped MoS_2 (including 28 S, 4 P, and 16 Mo atoms) to reduce the interaction from periodic boundary conditions as much as possible. For a single Na^+ ion adsorption on the monolayer MoS_2 , three different adsorption sites are available, namely, M site (top site directly above Mo atom), S site (top site directly above S atom), and H site (hollow site above the center of the hexagon). To compare energetics of the above three adsorption sites, we defined the formation energy of Na-ion adsorption as

$$E_f = [E(x_2) - E(x_1) - (x_2 - x_1)E_{Na}] / (x_2 - x_1) , \quad (5)$$

where $E(x_2)$ and $E(x_1)$ are the total energies of the Na_xMoS_2 compound or $\text{Na}_x(\text{P-doped MoS}_2)$ at two adjacent low-energy concentrations x_2 and x_1 . E_{Na} is the cohesive energy of Na in a body centered cubic (bcc) phase. Based on the above definition, a negative value implies that Na dispersively distributes on the MoS_2 basal plane. By contrast, a positive value implies that Na-ions on the MoS_2 surface prefers to cluster and that Na-metal will be formed during cycling. This scenario is not allowed in real applications. The formation energies of above three atomic configurations are obtained and listed in Table S1. Our results show that the M site is the most stable site, in agreement with previous reports.^[13] Therefore, only M sites are considered for the case of pure MoS_2 in our present work. For P-doped MoS_2 , the P site (top site directly above P atom), in addition to the above three sites, is also considered for Na^+ adsorption. Similarly, by comparing the calculated total energies of the four configurations (Table S1), we found that the M sites remain the most stable

sites for Na^+ ion adsorption. Interestingly, the formation energy is substantially lowered for the P-doped case, thereby implying that P-doping is beneficial to Na-ion intercalation on the MoS_2 .

Table S1. Formation energy of Na-ion adsorption at different sites on MoS_2 without and with P-doping.

	Sites	ΔE (eV)
Pure MoS_2	M	-0.214
	S	-0.180
	H	-0.186
P-doped MoS_2	M	-2.047
	S	-2.024
	H	-2.022
	P	-2.024

To obtain the maximum concentration of Na-ion intercalation on pure MoS_2 and P-doped MoS_2 , we continuously added Na^+ ions on the MoS_2 basal plane until the formation energy transforms from negative to positive. Na^+ ions were first placed at M sites to form the compounds of Na_xMoS_2 and $\text{Na}_x(\text{P-doped MoS}_2)$. Experimental results indicate that different Na intercalation concentrations in Na_xMoS_2 and $\text{Na}_x(\text{P-doped MoS}_2)$ were considered with x ranges from 1 to 5. The formation energies of different Na-ion concentrations x are calculated and listed in Table S2, which shows that the formation energies become positive value when $x = 4$ and 5 for Na_xMoS_2 and $\text{Na}_x(\text{P-doped MoS}_2)$ cases, respectively. This shows that the P-doping can improve the theoretical capacity of the MoS_2 by ~33%.

Table S2. Formation energy (E_f) of different Na concentration on MoS₂ without and with P-doping.

		E_f (eV)
	Na _x MoS ₂	Na _x (P-doped MoS ₂)
1	-0.745	-0.616
2	-0.526	-0.631
x	3	-0.102
	4	0.010
	5	—
		0.039

To further understand the energy barriers, we evaluated the Na-ion diffusion coefficients with the calculated energy barriers from the transition state theory, and the diffusion coefficient can be expressed as:^[14]

$$D = l^2 \nu_0 \exp(-E_a / k_B T), \quad (6)$$

where E_a is the migration energy barrier, k_B and T are the Boltzmann constant and absolute temperature, respectively; and l is the Na-ion migration distance. The vibrational frequency ν_0 is chosen to be approximately 10¹³ Hz. With these parameters, the Na ion/vacancy diffusion coefficients of MoS₂ and P-doped MoS₂ are evaluated and presented in Table S3.

Table S3. Theoretically calculated Na ion/vacancy diffusion coefficients of MoS₂ and P-MoS₂

	E_a (eV)	Diffusion coefficient (cm ² s ⁻¹)	
		T=273 K	T=298K
Na ion	MoS ₂	0.088	3.80×10 ⁻⁴
	P-MoS ₂	0.10	2.28×10 ⁻⁴
Na vacancy	MoS ₂	0.11	1.49×10 ⁻⁴
	P-MoS ₂	0.19	4.97×10 ⁻⁶

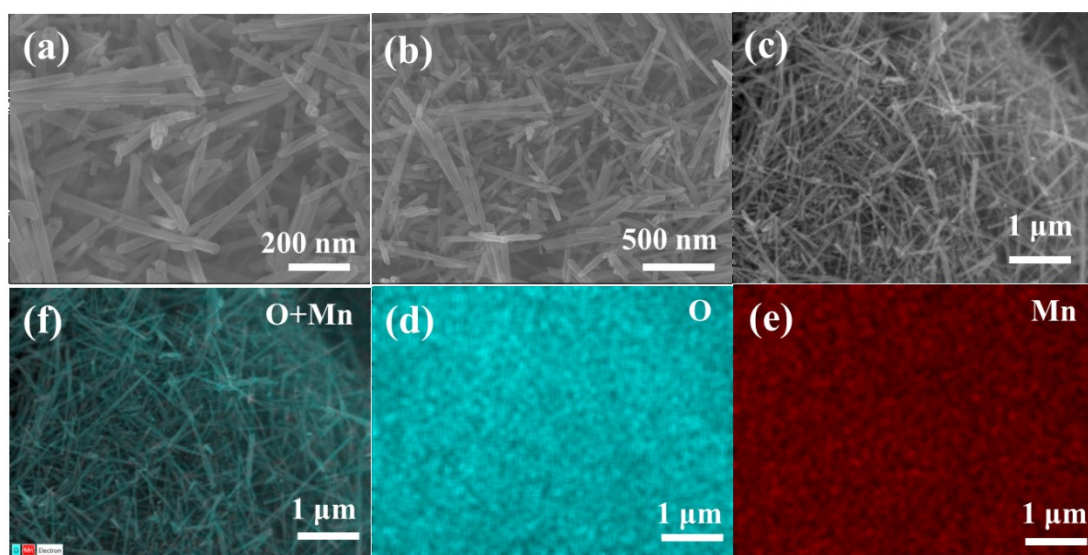


Figure S14. (a–c) SEM images of MnO₂ nanorods at different magnifications. (d–f) EDS elemental mappings of O and Mn elements recorded from image (c).

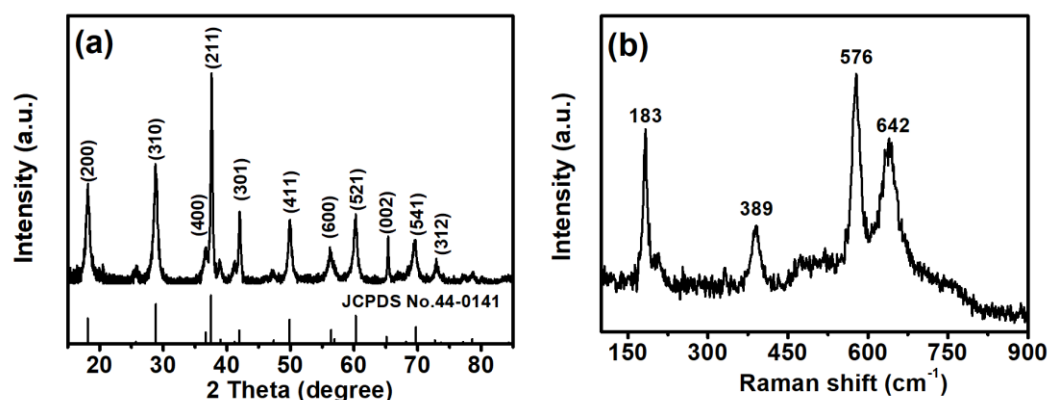


Figure S15. (a) XRD pattern and (b) Raman spectrum of MnO₂ nanorods.

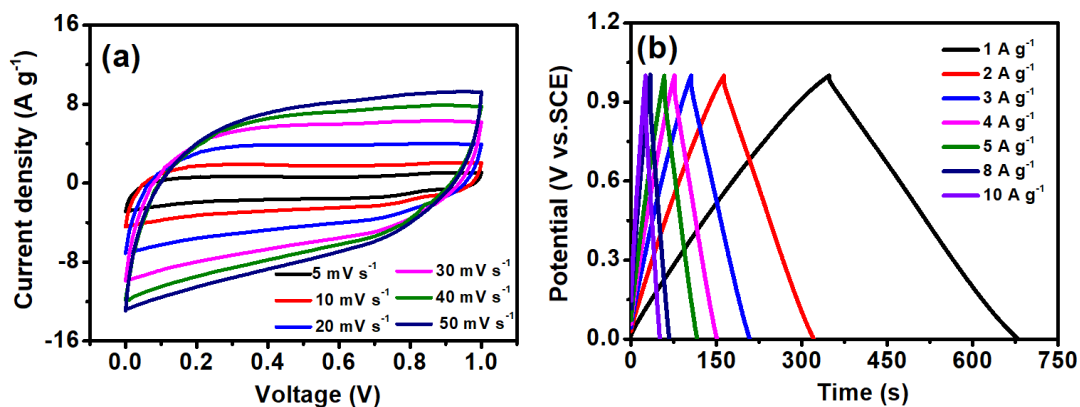


Figure S16. (a) CV curves at different scan rates, and (b) GCD curves at different current densities for MnO₂ nanorods.

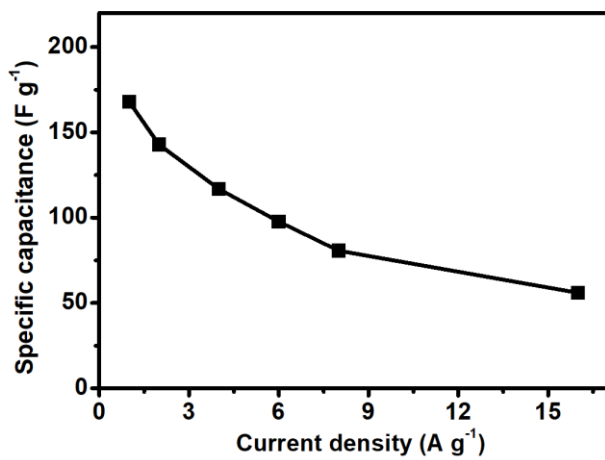


Figure S17. Gravimetric specific capacitance of the P-doped $\text{MoS}_2/\text{MnO}_2$ ASC device at various current densities.

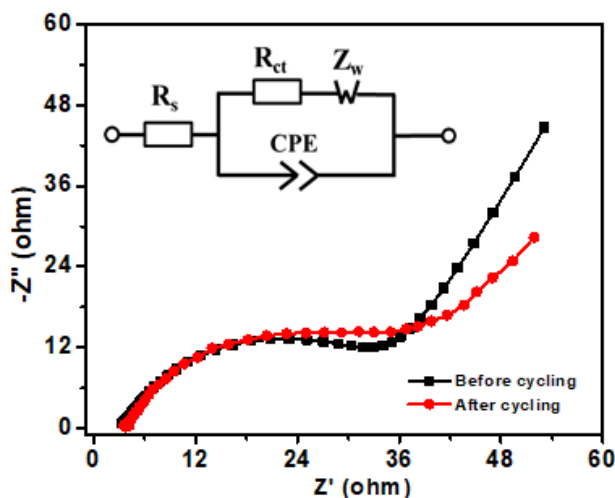


Figure S18. EIS plots of P-doped $\text{MoS}_2/\text{MnO}_2$ ASC device before and after 5000 cycles.

References

- [1] S. Zhu, L. Li, J. Liu, H. Wang, T. Wang, Y. Zhang, L. Zhang, R. S. Ruoff and F. Dong, *ACS Nano*, 2018, **12**, 1033-1042.
- [2] S. Liu, Y. Yin, K. S. Hui, K. N. Hui, S. C. Lee and S. C. Jun, *Adv. Sci*, 2018, **5**, 1800733.
- [3] H. Liang, C. Xia, A.-H. Emwas, D. H. Anjum, X. Miao and H. N. Alshareef, *Nano Energy*, 2018, **49**, 155-162.
- [4] S. Liu, D. Ni, H.-F. Li, K. N. Hui, C.-Y. Ouyang and S. C. Jun, *J. Mater. Chem. A*, 2018, **6**, 10674-10685.
- [5] P. E. Blöchl, *Phys. Rev. B*, 1994, **50**, 17953.
- [6] G. Kresse and J. Furthmüller, *Phys. Rev. B*, 1996, **54**, 11169.
- [7] J. P. Perdew, K. Burke and M. Ernzerhof, *Phys. Rev. Lett*, 1996, **77**, 3865.
- [8] H. J. Monkhorst and J. D. Pack, *Phys. Rev. B*, 1976, **13**, 5188.
- [9] S. Grimme, J. Antony, S. Ehrlich and H. Krieg, *J. Chem. Phys*, 2010, **132**, 154104.
- [10] G. Henkelman, B. P. Uberuaga and H. Jónsson, *J. Chem. Phys*, 2000, **113**, 9901-9904.
- [11] K. F. Mak, K. He, C. Lee, G. H. Lee, J. Hone, T. F. Heinz and J. Shan, *Nat. Mater*, 2013, **12**, 207.
- [12] S. Lebegue and O. Eriksson, *Phys. Rev. B*, 2009, **79**, 115409.
- [13] P. Rastogi, S. Kumar, S. Bhowmick, A. Agarwal and Y. S. Chauhan, *J. Phys. Chem. C*, 2014, **118**, 30309-30314.
- [14] Y. Chen, C. Ouyang, L. Song and Z. Sun, *Electrochim. Acta*, 2011, **56**, 6084-6088.